Alma Mater Studiorum Università di Bologna
Archivio istituzionale della ricerca

Understanding photocapacitive and photofaradaic processes in organic semiconductor photoelectrodes for optobioelectronics

This is the final peer-reviewed author's accepted manuscript (postprint) of the following publication:

This version is available at: https://hdl.handle.net/11585/893568 since: 2023-04-21

Published:

Terms of use:

(Article begins on next page)

Understanding Photocapacitive and Photofaradaic Processes in Organic Semiconductor Photoelectrodes for Optobioelectronics

Tommaso Paltrinieri, Luca Bondi, Vedran Đerek, Beatrice Fraboni, Eric Daniel Głowacki, and Tobias Cramer*

T. Paltrinieri, L. Bondi, Prof. B. Fraboni, Prof. T. Cramer
Department of Physics and Astronomy, University of Bologna, 40127 Bologna, Italy
E-mail: tobias.cramer@unibo.it

Dr. V. Derek
Department of Physics, Faculty of Science, University of Zagreb, Bijenička c. 32, 10000 Zagreb, Croatia

Dr. E. Głowacki
Laboratory of Organic Electronics, ITN Campus Norrköping, Linköping University, SE-60174, Norrköping, Sweden
Central European Institute of Technology, Brno University of Technology, Purkynova 123, 61200 Brno, Czech Republic

Abstract: Photoactive organic semiconductor substrates are envisioned as a novel class of bioelectronic devices that transduce light into stimulating biological signals with relevance for retinal implants or guided cellular differentiation. The direct interface between the semiconductor and the electrolyte gives rise to different competing optoelectronic transduction mechanisms. A detailed understanding of such faradaic or capacitive processes and the underlying material science is necessary to develop and optimize future devices. Here we address the problem in organic photoelectrodes based on a planar p/n junction containing phthalocyanine (H_2Pc) and *N,N'*-dimethyl perylenetetracarboxylic diimide (PTCDI). We combine the detailed characterization of photoelectrochemical current transients with spectroscopic measurements, impedance spectroscopy, and local photovoltage measurements to establish a model that predicts quantitatively faradaic or capacitive current transients. The decisive elements of the model are the energy levels present at the interface and the voltage building up in the photoelectrode. The result of our efforts is a comprehensive model of photocapacitive and photofaradaic effects that can be applied to developing wireless bioelectronic photostimulation devices.

1. Introduction:

Organic semiconductors are attracting increasing interest as photoactive substrates for the stimulation of biological cells and tissue.[1,2] Exposure to light efficiently generates excitons in organic semiconductors and localizes the electromagnetic energy of the radiation in close vicinity to the biological interface. Depending on the type of semiconductor and the interfaces present, the excitons can release the excess energy either by recombination into local heat or else by separating into a charge-separated state that initiates further electrical or electrochemical processes.[1] The thermal as well as the optoelectronic pathway both lead to a variation in local physicochemical properties of the illuminated photoactive substrate with possible impact on the biochemistry or bioelectronics of nearby cells. Thus, photoelectrodes offer a means to trigger optically a biological response with high temporal and spatial resolution and without the need for invasive wires to connect external power sources. First proof-of-principles applications that exploit this optoelectronic transduction pathway with organic semiconductors have been realized and regard optical stimulation of neurons for retinal implants,[3–5] optical activation of differentiation pathways for regenerative medicine[6,7] and modulation of neuronal signaling in in-vitro cultures.[8]

In addition to enabling an optical transduction pathway, a range of properties make organic semiconductors interesting candidates for photoactive substrates in biomedical applications.[2,9] As organic semiconductors are molecular or polymeric materials, they can be designed to offer soft mechanical properties allowing integration into flexible or stretchable devices.[10–12] The consequence is a better adaptation to curved biological formfactors and a larger compliance to the mechanics of biological tissue, both improving the interface quality and reducing invasiveness.[13] Also, for many organic semiconductors biocompatibility with different cell types has been demonstrated.[14–16] Finally, organic semiconductors offer stable electrochemical properties when in direct contact with aqueous electrolyte and a dielectric encapsulation layer can be avoided.[17,18] Hence extremely low-impedance interfaces between the electronic processes in the semiconductor and the ionic ones in the

cellular environment have been realized.[19] The low-impedance properties are at the core of many emerging organic semiconductor based bioelectronic devices such as organic electrochemical transistors[20] or low-invasive recording and stimulation arrays[13,21].

In photoelectrodes the direct interface between the semiconductor and the electrolyte opens several physicochemical pathways for light activated stimulation.[1] Photoexcited states can directly participate in electrochemical reactions in the nearby cell medium and organic semiconductors have been reported to show photocathodic[22–24] or photoanodic[25,26] reactions in aqueous electrolytes. A well-documented effect regards the reduction of dissolved oxygen to hydrogen peroxide by photoactivated electrons.[27,28] At variance to such faradaic reactions is photocapacitive behavior.[5] In this case, no electrons are transferred across the semiconductor/electrolyte interface. Instead excitons dissociate into a charge separated state at an internal interface such as the semiconductor/metal electrode or a p/n heterojunction. This causes an ionic displacement current until the electric field of the charge separated dipole is screened. Photofaradaic and photocapacitive effects impact very differently on biological cells. Reactive oxygen species formed during faradaic reactions have been demonstrated to impact on the cell's biochemistry causing alterations in intracellular calcium level and inflammation reactions at higher concentrations.[6,7] Instead photocapacitive currents vary locally the cell's membrane potential[29] and can trigger action potentials in neurons.[5] Clearly, effective photoelectrodes must enable a single stimulation mechanism, based on either photofaradaic or photocapacitive transduction. However, to date it is not clear whether such a strict separation can be achieved in photoelectrodes based on organic semiconductor in direct contact with the electrolyte. Progress will require a detailed understanding about how the photoelectrode architecture and the semiconductors electronic material properties impact on photocapacitive versus photofaradaic processes.

To address this problem, we report here detailed photoelectrochemical characterizations and theoretical analysis on photoelectrodes with a phthalocyanine (H$_2$Pc) and perylenetetracarboxylic

diimide (PTCDI) heterojunction. Such photoelectrodes have been demonstrated to work as effective photocapacitors that enable the stimulation of retinal neurons or single cell oocytes in in-vitro experiments.[5,29] At the same time PTCDI based photoelectrodes have also been reported to act as photocathodes with strong faradaic reactions yielding effective hydrogen peroxide generation.[27,28] In H_2Pc/PTCDI heterojunctions, this faradaic process is enhanced when electron donors such as glucose are present to close the electrochemical cycle with anodic oxidation at the back-electrode.[30] Based on these to-date findings, the H_2Pc/PTCDI heterojunction photoelectrode represents a model system with both photocapacitive as well as photofaradaic behaviour. The factors affecting the prevalence of either regime remain ambiguous and quantitative understanding of transient photocurrent signals is currently missing. We address this issue by combining transient and spectroscopic photocurrent measurements with electrochemical impedance spectroscopy and microscopic characterizations on H_2Pc/PTCDI photoelectrodes. Our findings lead to an equivalent circuit model that reproduces quantitatively photocurrent transients and explains the transition between capacitive and faradaic behavior. The model shows how intrinsic material properties such as semiconductor energy-levels and reorganization energy determine photocurrent signals and how the photoelectrode geometry can be tuned to control and optimize photocurrent generation. The model can easily be extended to more complex photoelectrode operation modes. As examples we explain the large electrochemical photovoltage generation observed in the photoelectrodes and rationalize the impact of the back-electrode in floating photocapacitor pixels for wireless operation, such as in retinal stimulation applications.

2. Results:

2.1. Faradaic and capacitive photoelectrode processes

Figure 1a depicts a scheme of the basic experiment used to characterize photoelectrodes made of an indium tin oxide (ITO) substrate onto which an organic planar heterojunction of p-type H_2Pc (30 nm) and n-type PTCDI (30 nm) were thermally evaporated. The border of the photoelectrode is sealed by

a silicone o-ring to expose an area of 0.785 cm^2 diameter to the aqueous electrolyte (0.1 M phosphate buffered saline - PBS). A potentiostat connected to the ITO substrate (WE) and to the Ag/AgCl reference electrode (RE) and Pt-wire counter electrode (CE) controls the voltage V_r applied to the photoelectrode with respect to reference in the electrolyte and measures transient photocurrents. The Figure also shows schematically the basic mechanisms that can contribute to photocurrent signals. Upon illumination, excitons are generated in the organic semiconducting layer and separate into holes and electrons at the planar p-n junction. The separated charge carriers can follow two principally different reaction pathways to contribute to the photocurrent transient. First, charge separation into positive and negative carriers in the p-type and n-type layer, respectively, gives rise to an electric field that attracts cations to the surface and repels anions. In this way a transient ionic displacement current I_C is generated in the electrolyte that persists until the ionic double layer at the semiconductor/electrolyte interface is charged. This capacitive mechanism is indicated by a blue arrow in Figure 1c. Second, free electrons in the n-type layer can tunnel onto acceptor molecules in the liquid and give rise to reductive faradaic processes. A typical acceptor state in ambient conditions regards dissolved oxygen.[28,31] This faradaic current I_F does not cause the accumulation of charges at the interface, as both, the remaining hole charge as well as the negatively charged acceptor, are free to diffuse away from the interface. Consequently, a constant steady current is generated from the faradaic process, as long as mass transport of acceptor molecules does not become limiting. This mechanism is indicated by the red arrow in the Figure 1a.

Figure 1b shows two photocurrent transients measured at different photoelectrode voltages. The two transients are presented here as the first evidence that both, capacitive as well as faradaic mechanism coexist and can be controlled by external parameters. When applying a positive voltage ($V_r = 0.25$ V), a negative current spike is observed at the onset of illumination (590 nm, 12.4 mW/cm^2), corresponding to the formation of a positively charged ionic layer at the photoelectrode surface. Upon switching off the light, the double layer discharges and a similar current spike of positive sign is present. In contrast, at negative photoelectrode voltage ($V_r = -0.15$ V) an almost constant negative

current is observed during illumination and no current spikes are generated. Consequently, the current is caused purely by the faradaic process and no variation in double layer charge occurs.
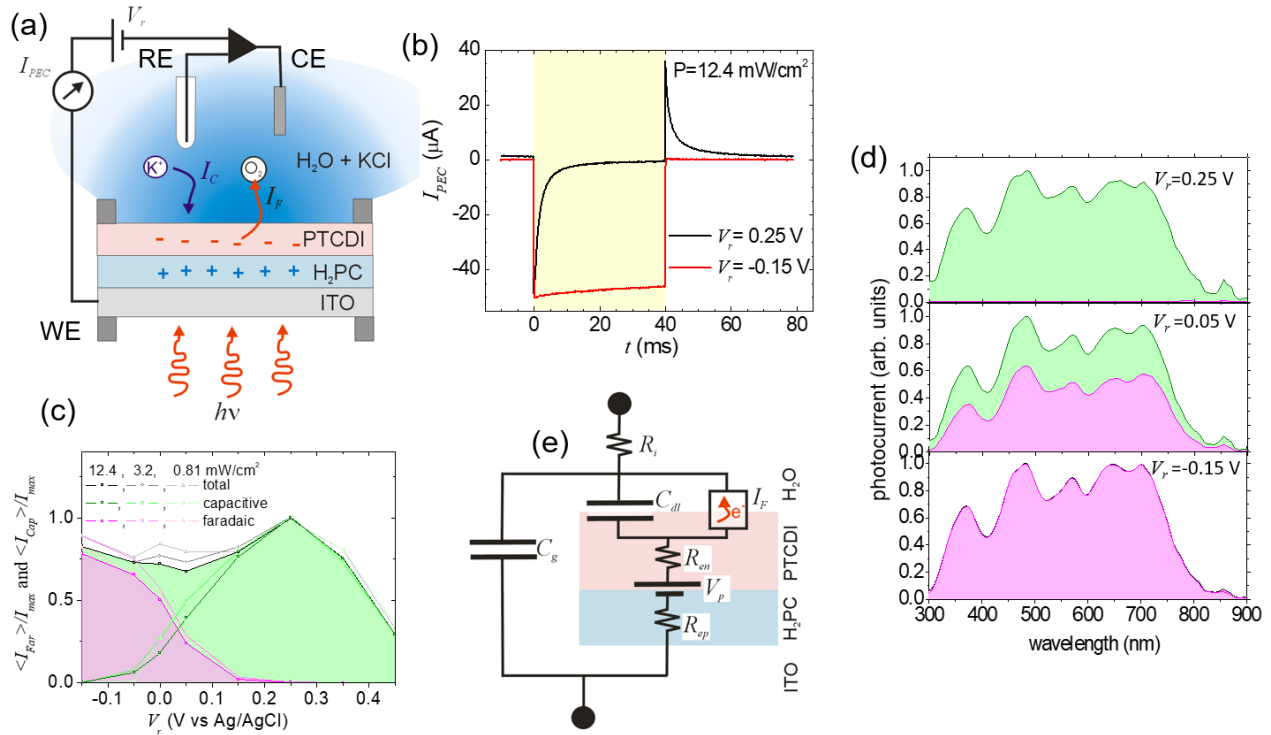

Figure 1. Capacitive and faradaic currents in organic photoelectrode. (a) Scheme of the experiment. Optically evoked capacitive currents I_C involve ionic displacement currents as indicated by the blue arrow. Faradaic currents I_F instead involve an electron transfer from the electrode onto oxygen, that acts as an electron acceptor in solution. (b) Current transients acquired during an illumination cycle (595 nm, 12.4 mW/cm^2) for two different voltages V_r applied to the working electrode. At positive voltages, the transient shows characteristic features of a capacitive mechanism. At more negative voltages, a faradaic behaviour is observed. (c) Ratio of capacitive and faradaic current contributions as a function of the voltage and in (d) as a function of excitation wavelength. (e) equivalent circuit proposed to model the photoelectrode. Crucial elements are the double layer capacitance of the photoelectrode C_{dl}, a voltage source simulating the photovoltage V_p generated at the p/n junction, an element describing faradaic charge transfer I_F and the resistance of the semiconducting layers R_e.

To distinguish faradaic from capacitive currents quantitatively we compute the net total charge transferred across the photoelectrode interface per illumination cycle by integrating over the current transient:

$$Q_F = \int_{t=0}^{T} I(t)dt \qquad (1)$$

The resulting number is the total amount of faradaic charge Q_F assuming an irreversible electron transfer process. Instead capacitive displacement currents cancel each other out in this integral as they appear with both, positive and negative polarity. To count capacitive charges Q_C we have to consider the absolute value of the current transient and subtract the amount of faradaic charge:

$$Q_C = \frac{1}{2}\left(\int_{t=0}^{T}|I(t)|dt - |Q_F|\right) \tag{2}$$

From the charges Q_F and Q_C we define average photocurrent values as $<I_F>=Q_F/T$ and $<I_C>=Q_C/\tau$, where T is the period of the illumination cycle and τ is the characteristic time constant describing the capacitive transient decay time (see Suppl. Inf. S1). Figure 1c plots the average faradaic and capacitive photocurrents as well as the total averaged photocurrent $<I_F> + <I_C>$ as a function of photoelectrode voltage V_r. The plot demonstrates the fundamental role of the electrochemical voltage V_r for controlling the transients at the semiconducting photoelectrodes. At positive voltages we observe purely capacitive behavior. The transition to a faradaic regime sets in at 0.1 V and until -0.1V both mechanisms coexist. Below this voltage a purely faradaic regime is observed. In a similar experiment we investigated the impact of the excitation wavelength on the ratio between faradaic and capacitive processes. Figure 1d shows photocurrent spectra obtained at three different voltages. In the positive range, the spectrum constitutes only capacitive current contributions, while at negative voltages the processes are almost entirely faradaic. Despite the change in mechanism, the overall shape of the spectra remains unaltered and the ratio of capacitive to faradaic processes is not influenced by the wavelength. The finding clearly demonstrates that the electrochemical reactions happen on a slower time scale and only depend on the number of charges separated at the p-n junction. The energetics and dynamics of exciton formation and separation as well as charge transfer state relaxation dynamics are much faster and do not have a direct impact on the following electrochemical process.

Based on these findings and on the qualitative understanding of the p-n junction photoelectrode we propose the equivalent circuit depicted in Figure 1c to arrive at a quantitative model. The circuit is

composed of a voltage source that represents the dipole and associated photovoltage V_p present at the p-n junction during illumination. Transport of electronic carriers across the semiconductor is described by the resistances R_{ep} and R_{en}. In the electrolyte the transport of ions is modelled by the resistance R_i. The semiconductor/electrolyte interface is modelled by two elements: first, a capacitance C_{dl} that represents the double layer containing electronic charges in the semiconductor and ionic charges in the electrolyte. Second, a non-linear element that causes the faradaic charge transfer processes I_F. Finally, a smaller capacitance C_g is put in parallel to the circuit to account for the geometric capacitance of the organic semiconductor layer. Clearly, this circuit is simplified but it allows to grasp the most relevant processes at the p-n or ITO-p interfaces. In the following, we provide a characterization for each individual circuit element based on electrochemical impedance spectroscopy and photovoltage measurements. Only then we turn back to transient behavior and apply the parametrized circuit to achieve a quantitative description of the current transients.

2.2 Surface photovoltage measurements: Electrical stimulation with the photoelectrode is driven by photovoltage generation. In the equivalent circuit model this process is attributed to the p-n junction and in first approximation independent on the presence of electrolyte. To confirm this hypothesis and to arrive at quantitative photovoltage values that characterize the voltage source in the equivalent circuit we perform Kelvin-Probe Force Microscopy (KPFM) on photoelectrode/air interfaces in darkness and during illumination. **Figure 2a, b and c** show, respectively, images of the surface height, workfunction, and surface photovoltage V_p obtained from such measurements. The surface topography is dominated by the nanocrystalline structure of the evaporated organic semiconductor with crystallite sizes on the order of $10 - 20$ nm. The workfunction is close to the level of the underlying substrate (ITO) and reveals that in darkness interfacial dipoles due to thermally activated charge transfer states are not present.[32] Upon illumination, we observe the formation of a negative photovoltage. The precise values of both, workfunction as well as photovoltage, depend strongly on the local topography. The profiles of height, workfunction, and surface photovoltage in Figure 1d obtained from the images show the effect more clearly. Overall, the length scale of the

local fluctuations match to variations in surface height. Therefore, we suggest that changes in nanocrystallite orientation are responsible for the variations in workfunction and surface photovoltage. We note that the length scale of the surface photovoltage fluctuations is however orders of magnitude below the typical size of cells. Therefore, we consider the average photovoltage to be relevant for photoelectrode biological activity (and not the local fluctuations). Figure 1e then shows how the average photovoltage increases with light intensity P. At relatively low light intensities of $P=3$ mW/cm^2 we observe photovoltages exceeding 30 mV. For strong cell-photoelectrode contacts with high sealing resistance, such a value can already be sufficient for cell membrane depolarization. Higher light intensities lead to even stronger photovoltage response as required for efficient cell depolarization.[29] The inset of the Figure shows the photovoltage transient and confirms the fast rise and decay times of the photovoltage ($\ll$ 1ms). The functional dependence of photovoltage on light intensity is described by a logarithmic function similar to photovoltages observed in inorganic heterojunctions.[33]
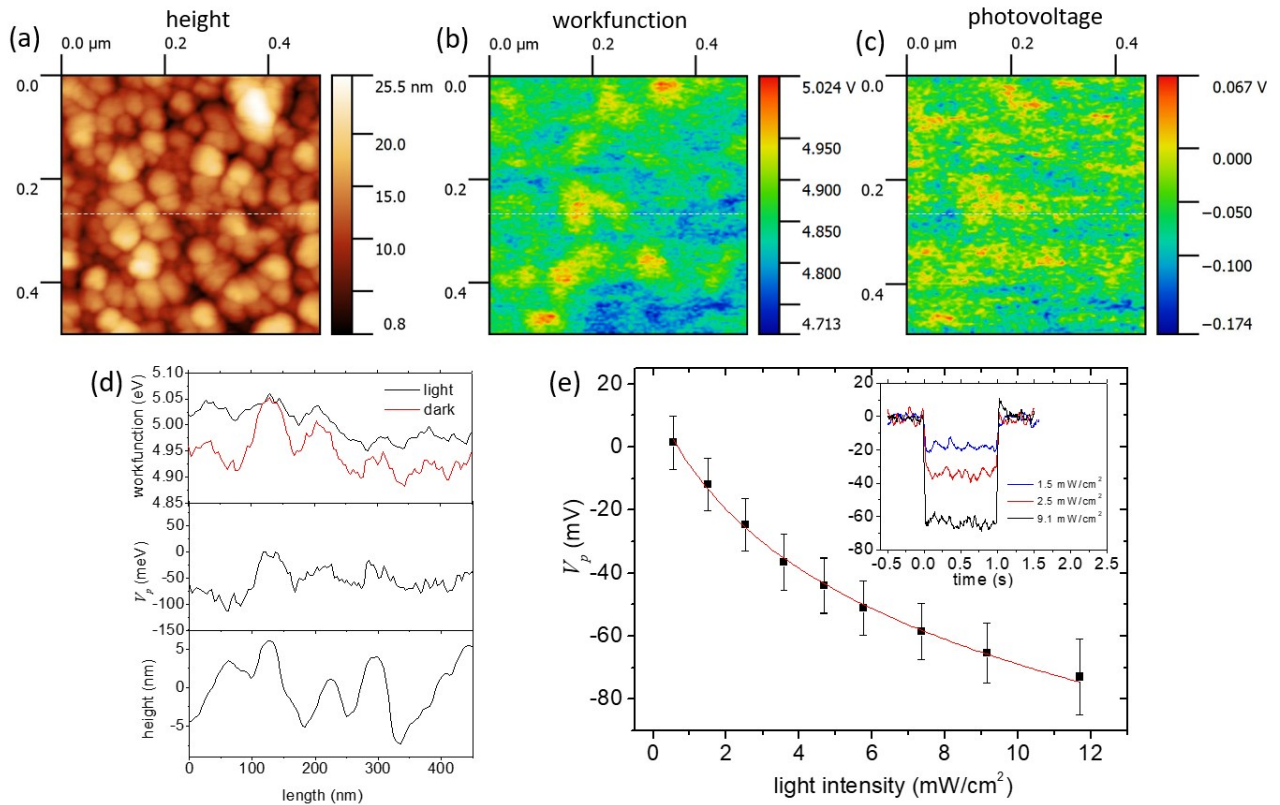
Figure 2. Kelvin Probe Force microscopy (KPFM) on the photoelectrode surface. (a) Topography of sample (b) local workfunction calculated from KPFM potential in darkness. (c) local photovoltage V_p calculated from KPFM potential measured during illumination and darkness. (d) Line profiles of the images. (e) Averaged KPFM photovoltage as a function of light intensity. The inset shows typical measurement transients.

2.3 Electrochemical impedance spectroscopy: EIS performed in darkness and during illumination provides quantitative data describing passive elements in the photoelectrode equivalent circuit. Bode plots of impedance and phase measured at different photoelectrode voltage V_r are shown in **Figure 3a** and b. As EIS measures the passive circuit properties we do not consider the voltage source in the model to fit the measurement data. Due to the small modulation amplitude the faradaic element is treated as a charge transfer resistance R_{CT}. All other elements in the fitting model are kept as depicted in Figure 1d. The resulting fit describes well the experimental data and we obtain quantitative values for C_{dl}, C_g, R_{Ct}, R_i and $R=R_{ne}+R_{np}$. In darkness, the heterojunction behaves as a dielectric and the impedance response is dominated by the geometric capacitance C_g and the ionic resistance R_i. This is a direct consequence of the fact that the organic materials are intrinsic, undoped semiconductors with

very low conductivity in the dark. During illumination, the impedance drops by orders of magnitude and typical features appear in the amplitude and phase spectra that are well reproduced by the simple model circuit. Deviations between model and measured data are only notable in the EIS phase spectra at positive photoelectrode voltages (V_r>0.15). At these voltages, the peak associated to the double layer capacitance broadens. This disagreement between model and data is associated to positive charge carriers that migrate from the ITO electrode into the p-type layer and are subjected to disorder and surface roughness at the ITO/H_2Pc interface which is not considered in our idealized model.
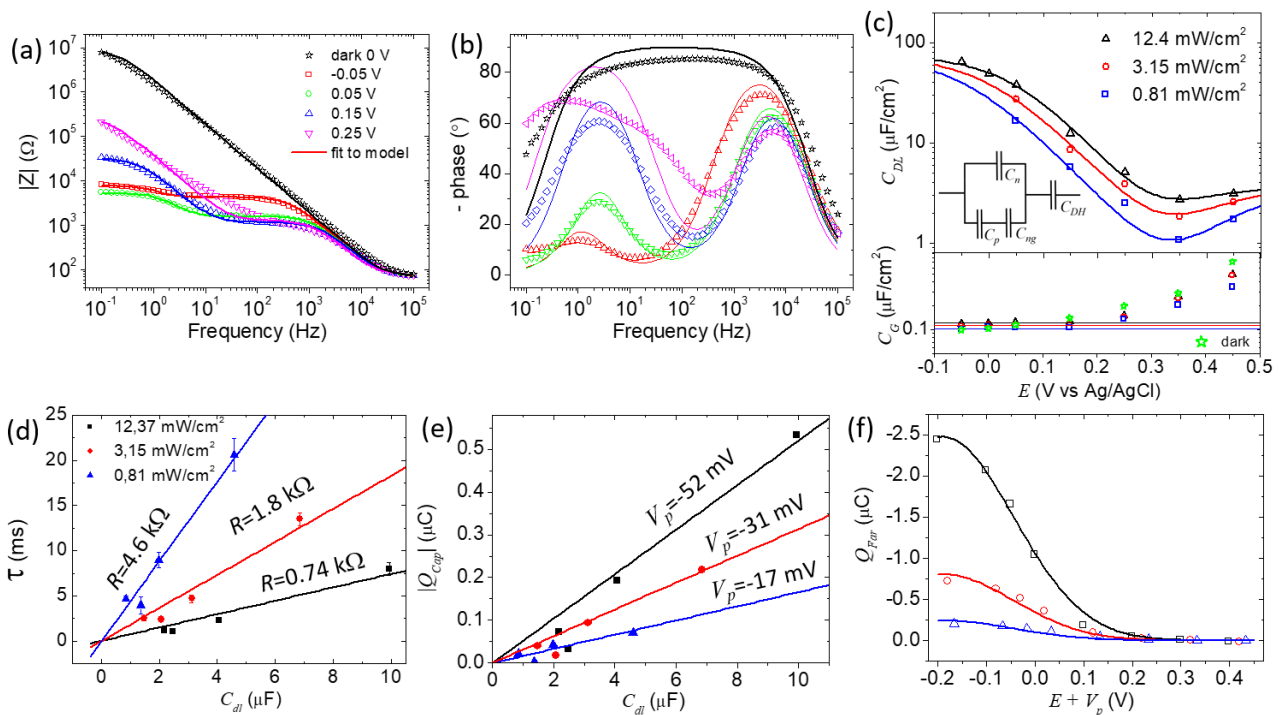

Figure 3. Determination of parameters for photoelectrode equivalent circuit. (a,b) Electrochemical impedance spectroscopy data and fit to model. Data measured in darkness and during illumination at 595 nm with 12.4 mW/cm^2 at different voltages V_r. (c) Extracted double layer capacitance and geometric capacitance as a function of V_r. Solid lines show fits to capacitance models as detailed in the text. (d) Plot of capacitive photocurrent time constant τ as a function of double layer capacitance C_{dl} to determine the characteristic resistance R of the junction. (e) plot of capacitive charge Q_C as a function of C_{dl} to determine the photovoltage V_p. (f) Plot of faradaic charge Q_F as a function of effective voltage $V_r + V_p$ and fit to Marcus-Gerischer model describing faradaic charge transfer.

Most importantly, the EIS model provides access to C_{dl} and C_g of the photoelectrode. Figure 3c shows these capacitances normalized per photoelectrode area as a function of photoelectrode voltage. The geometric capacitance C_g is independent on light intensity and shows almost no dependence on V_r.

Only at larger positive photoelectrode voltage a slight increase in C_{dl} is observed which is attributed to hole carriers that start to enter into the p-type H_2Pc layer. Instead a strong dependence of the double layer capacitance C_{dl} on photoelectrode voltage and illumination power is present and variations exceeding an order of magnitude are observed. Maximized capacitance with values typical for the Debye-Helmholtz layer are only reached at negative voltages. Towards more positive voltages the value of C_{dl} drops by more than an order of magnitude. This effect can only be explained by an additional, strongly voltage dependent capacitance in series to the Debye Helmoltz capacitance C_{DH}. The semiconductor in direct contact with the electrolyte is the n-type PTCDI. Consequently, a more positive voltage applied to the photoelectrode causes a drop in the Fermi-level and reduces the number of negative carriers in the conduction band. The resulting decrease in capacitance for an undoped semiconductor is described by[34]:

$$C_n = A \frac{\varepsilon \varepsilon_0}{L_n} \exp\left(-\frac{qV_r}{ikT}\right) \tag{3}$$

with the intrinsic screening length L_n, dielectric constant ε and a non-ideality factor i. Only at very positive voltages the total measured capacitance starts to rise again. Now, positive charges in the close-by p-type H_2Pc layer start to accumulate and interact with the counterions in solution resulting in a capacitance that is a series combination of the undoped p-type semiconductor C_p, described by an equation similar to eqn. [3], and a geometric capacitance C_{ng} describing the depleted n-type PTCDI layer. The inset in Figure 3c shows how the different capacitances are combined in series and in parallel to achieve a quantitative fit to the capacitance data (see Suppl. Inf. S2 for more detailed description).

In the next step, we use the quantitative description of the capacitance C_{dl} to achieve a first estimation of the effective resistance R and photovoltage V_P of the heterojunction based on the PEC transient data. For transients in the capacitive regime ($V_r > 0.05$ V) we plot in Figure 3d and 3e the characteristic time constant τ and the total charge stored on the double layer capacitor Q_C as a function of C_{dl}. In both cases the linear fit to the data confirms the simple capacitor relations $Q_C = V_p \cdot C_{dl}$ and $\tau = R \cdot C_{dl}$

allowing to extract R and V_p values for different light intensities. Notably, the photovoltage values V_p are in good agreement with the KPFM based measurements and confirm our initial hypothesis that the photoelectrode is driven also in electrochemical environment by exciton separation at the p-n junction.

The last missing element regards the faradaic processes. In Figure 3c we plot the faradaic charge extracted from the PEC transient as a function of photoelectrode voltage. For the three different light intensities a similar functional dependence is obtained that shows the onset of faradaic processes at 0.1 V and exhibits a strong increase towards negative voltages until a saturation is reached. The stable current plateau in the PEC transient and the CV-data (see Suppl. Inf. S3) indicates that the process is not limited by mass transport. Instead the heterojunction resistance in series with the charge transport process on the acceptor state dominate the current. We thus model the rate limiting process of the oxygen reduction reaction by applying a Marcus-Gerischer rate equation leading to the expression:

$$Q_F = \Delta t \cdot I_F = \Delta t \cdot I_{F,0} \, exp\left[-\frac{\left(\Delta G^0 + qV_r - I_F R + V_p + \lambda\right)^2}{4\lambda kT} \right] \tag{4}$$

In which I_F is the faradaic current, Δt is the duration of the light excitation, λ is the reorganization energy, and ΔG^0 the free energy of the charge transfer process. Eq. 4 depends recursively on the current I_F that passes through the heterojunction of resistance $R = R_{ne} + R_{np}$ as it creates an additional potential drop across the photoelectrode. A solution for eq. 4 was obtained numerically. For the different light intensities, we varied only the prefactor $I_{F,0}$ and obtain excellent fits to the data (lines in Figure 3c) with an overall reorganization energy of $\lambda = 0.43 \pm 0.07$ eV. Such a value is in the typical range for single electron CT processes at aqueous interfaces.[34] The free energy of the charge transfer process amounts to $\Delta G^0 = -0.24 \pm 0.04$ eV and represents the difference between the edge of the PTCDI conduction band and the standard potential of the oxygen acceptor state.

2.4 The full photoelectrode model

At this point we have numerical representations for all elements in the equivalent circuit of the photoelectrode. The combined set of differential equations describing the current flow is solved numerically using Runge-Kutta algorithm (see Suppl. Inf. S4). Measured and simulated transients are compared in **Figure 4** for different light intensities and photoelectrode voltages. The simulations that are based on the parameters obtained as described above (red curve in Figure 4) achieve a reasonable description of the relevant features in the transients such has the capacitive current spike at positive voltages and the transition towards pronounced faradaic currents during illumination at negative voltages. However, stronger differences between simulated and measured transients exist in the capacitive contribution at positive photoelectrode voltages. To improve the agreement, we introduce the photovoltage as a fitting parameter, that depends on the light intensity and also on the voltage V_r. This is justified by the strong impact of electric fields on recombination processes at the p-n heterojunction. For example, stronger photovoltages should be present at negative photoelectrode voltages where the electric field facilitates exciton splitting and charge separation. After the numerical fitting procedure, we obtain an almost quantitative agreement with the measured transients. The Suppl. Inf. S5 contains all the numerical values of the parameters/functionals used in the fit.
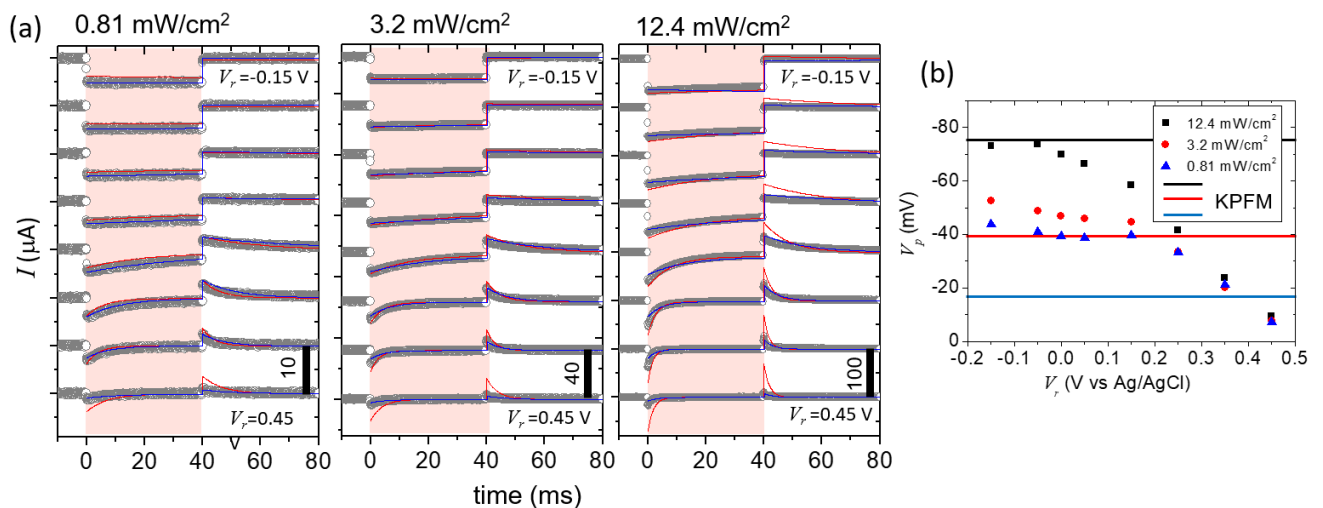

Figure 4. Measured (grey points) and simulated photocurrent transients (red and blue lines) obtained at different light intensities and photoelectrode voltages. For clarity transients with different photoelectrode voltage are shifted by an offset. The red lines correspond to the model with parameters determined *a priori* from EIS and photovoltage measurements. The blue line corresponds to the model optimized directly with the transient data using photovoltage and heterojunction resistance as fitting parameters.

With the full model in hand, we can arrive at important conclusions regarding the p-n heterojunction based photoelectrode. **Figure 5a** shows the energy diagram of the heterojunction in contact with the electrolyte in darkness. During illumination excitons are generated in the p-type and n-type layer. After diffusion to the junction the excitons separate into a hole charge in the valence band of the H_2Pc layer close to the ITO back electrode and an electronic charge in the conduction band of the PTCDI layer in contact with the electrolyte. The charge separation leads to the formation of the dipole layer at the p-n junction and generation of photovoltage. After charge separation, two reactions are possible and indicated in the energy diagram: In the first case, the electron interacts with counterions in the electrolyte and gives rise to the capacitive current pulse (blue arrow). Once the Debye-Helmholtz layer is established, no further current is generated and charge separation and recombination at the heterojunction occur at equal rate. In the second case, the free electron in the PTCDI conduction band can tunnel onto the O_2-acceptor state in the electrolyte (red arrow). As new charges are continuously generated in the heterojunction, this process gives rise to the steady faradaic current.

The efficiency of the tunneling process involved in the faradaic process depends strongly on the energetics of the involved states. From our measurements we obtain a free energy of ΔG^0=-0.24 eV. Combining this value with the electron affinity of PTCDI, $E_{A,PTCDI}$ = 4.1[35] and the PTCDI/PBS surface dipole in darkness estimated to be qV_d = 0.23 eV from KPFM measurements (see Suppl. Mat. S6), we obtain the energy level of the acceptor state, E^0_{OxRed}= $E_{A,PTCDI}$ + ΔG^0- qV_d = 4.11 eV. This value compares well to the standard potential of the rate limiting, one-electron oxygen reduction process leading to the superoxide radical anion $E^0_{O2/O2-}$ = 4.1 eV[36] and is significantly above the level for the two-electron process reported for the final reaction product hydrogen peroxide $E^0_{O2/H2O2}$ = 4.8 eV.[31]

The energy diagram explains the relevant factors that decide on capacitive or faradaic photoelectrode behaviour. A negative photoelectrode voltage V_r shifts the semiconductor levels upwards with respect to the oxygen acceptor level, thus making electron transfer more probable and causing a larger

faradaic current. Instead a positive voltage V_r supresses faradaic transfer as the acceptor state rises above the PTCDI conduction band level. From these findings we predict that the capacitive mechanism becomes favoured in semiconductors with lower conduction band levels (high electron affinity) and strong reorganization energy, whereas larger bandgaps and high lying conduction bands support the faradaic process.
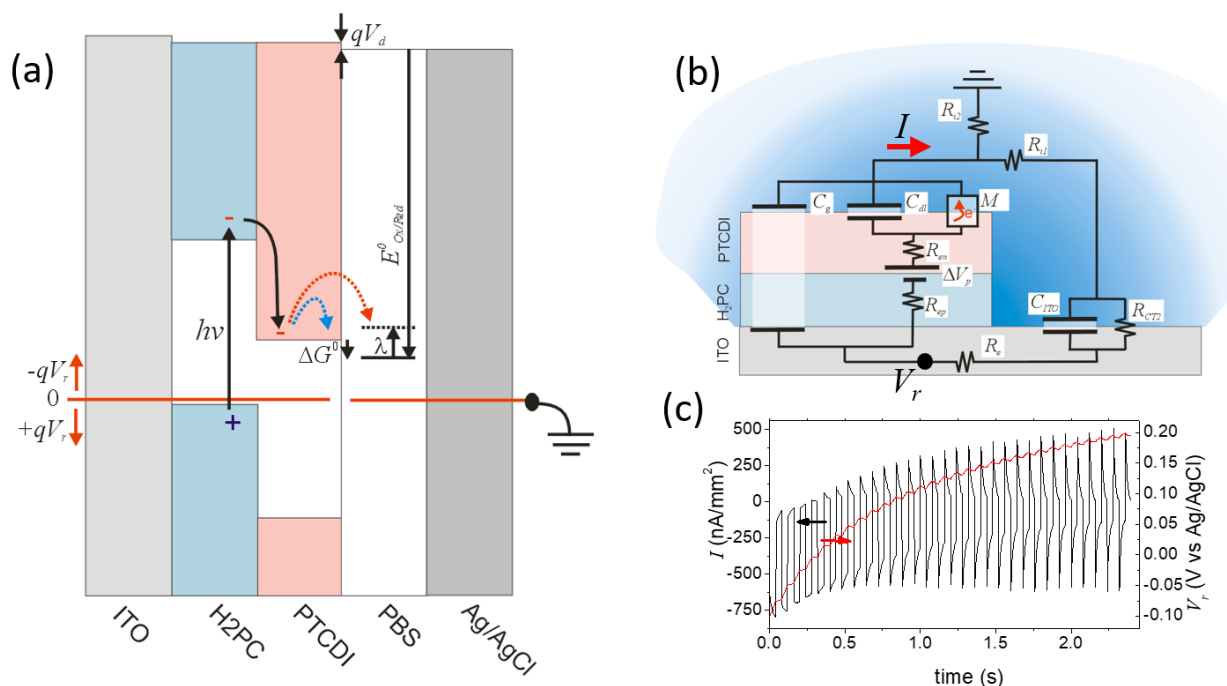

Figure 5. Implications of photocapacitor equivalent circuit model. (a) Energy diagram of photocapacitor junction in darkness and interpretation of capacitive and faradaic currents. The model provides estimates for the reorganization energy $\lambda = 0.43$ +/- 0.07 eV and for the free energy $\Delta G^0 = -0.24$ +/- 0.04 eV. (b) Equivalent circuit of floating photocapacitor pixel. (c) Simulated floating photocapacitor response showing transition from faradaic to capacitive operation regime without external control.

To highlight the relevance of the photoelectrode circuit model we employ it to simulate floating photocapacitor pixels. A floating configuration is important in bioelectronic applications as the pixel should activate by light without any wire attached. To provide a circular pathway for the generated current in a floating electrode pixel, the ITO back electrode must be put into direct contact with the electrolyte as shown in Figure 5b. The ITO/electrolyte interface is modelled by the resistance R_{ITO} and the capacitance C_{ITO}. The two elements are crucial as they close the circuit for photocurrent

generation in the floating electrode necessary to maintain charge balance. Values for both are obtained from EIS measurements on ITO. Experimentally, there is no way to measure or control the photoelectrode voltage Vr in the floating configuration. Thus, at first sight it might be unclear how to control capacitive or faradaic contributions in such a floating pixel. To understand the situation, we run simulations for the worst-case scenario for wireless stimulation: the photoelectrode is for some reason at a negative potential. As shown above, the negative potential should lead to a faradaic process, although a capacitive one would be desired to avoid reactive oxygen species to be generated. The simulation of such an initial condition with Vr=-0.1 V is shown in Figure 5d. As expected the simulated current transient shows in initially a faradaic shape. However, already after a few illumination pulses the shape changes and becomes charge balanced and capacitive. Accordingly, the Vr drifted from the negative initial condition to a stable positive value. Therefore, even in the worst case, a faradic mechanism cannot prevail on the floating photocapacitor pixel when ITO is employed as a back-electrode. The effect explains our earlier work in which H_2Pc-PTCDI based floating photoelectrodes behave as photocapacitors with charge balanced stimulation profiles that do not show faradaic current contributions. We note that the effect can be further influenced directly by the electro-chemical properties of the backelectrode such as the Nernst-potential.[30]

3. Conclusions

In this work we analyse in detail the photoelectrochemical processes that lead to photocurrent generation in organic heterojunction based photoelectrodes operated in contact with aqueous electrolyte. Electrochemical impedance spectroscopy, Kelvin probe force microscopy and spectroscopic photocurrent measurements are used to determine basic properties of the heterojunction/electrolyte interface such as photovoltage, capacitive coupling and charge transfer resistance. The findings are combined into an equivalent circuit model that is in quantitative agreement with measured photocurrent transients and provides a clear explanation for photocapacitive as well as photofaradaic processes. Photofaradaic processes, that are undesired in bioelectronic stimulations, can be avoided by applying positive voltage to the photoelectrode. In this

way electrons emerging out of charge separated states do not tunnel onto electrochemical acceptor states but remain in the conduction band and interact only electrostatically with the electrolyte generating an ionic displacement current. The equivalent circuit model relates the magnitude and the time constant of the displacement current to the double layer capacitance, the photovoltage generated at the organic p-n junction and the total resistance of the heterojunction. We further employ the model to provide important insight into the response of floating photoelectrodes as employed for retinal neuron stimulation. The simulation shows that in the floating configuration the photoelectrode automatically charges positively and operates in the purely capacitive mode.

We are convinced that our findings provide guidance for the design and optimization of future organic optobioelectronic interfaces. Our results demonstrate how semiconductor energy levels impact on capacitive or faradaic processes. To maximize the capacitive pathway exploited in artificial retina interfaces, transport properties of the heterojunction as well as electronic photovoltage generation have to be optimized. The equivalent circuit model presented here shows how these properties are interrelated and dependent on semiconductor material properties as well as device architecture.

4. Experimental Section/Methods

Photoelectrode fabrication: 15×15 millimeter square ITO slides (Kintec, 15-20 Ohm/sq) were cleaned by consecutive ultrasonication for 5 minutes in acetone, 2-propanol and 2% Hellmanex III cleaning solution. The substrates were then rinsed with DI water and dried under a stream of N_2. Next, O_2 plasma treatment was applied (100 W, 5 minutes) and the ITO surface was modified by a vapor-phase deposition of *n*-octyltriethoxysilane (OTS) by placing the samples in an OTS-vapor saturated chamber heated to 80 °C for 1 h. This improves the adhesion of organic PN layers to the ITO substrate. Excess physioadsorbed OTS was removed by sonicating the samples in acetone for 5 min followed by rinsing with DI water and drying under N_2 stream. Phthalocyanine H_2Pc (Alfa Aesar) and *N,N'*-dimethyl-3,4,9,10-perylenetetracarboxylic diimide, PTCDI (BASF) were purified thrice by temperature-gradient sublimation. The H_2Pc/PTCDI layers were formed by evaporative deposition at a base pressure of $< 2 \times 10^{-6}$ Torr using a rate of 0.1-0.5 nm/s. 30 nm of P-type H_2Pc and 30 nm of N-type PTCDI were successively deposited. Kapton tape was used to mask the edges of the ITO substrate to leave areas convenient for electrically contacting for later measurements. All samples were then stored in 0.1 M KCl for 24 h before further use.

Photoelectrode electrical characterizations: The photoelectrode was mounted in a homemade PEC-cell (design inspired from literature[37]). A silicone o-ring confined the photoelectrode area to a diameter of 10 mm in contact with aqueous electrolyte (PBS 0.1 M) and prevented electrochemical contact with the back ITO electrode. A Pt-wire and Ag/AgCl (3M KCl) reference electrode were used to control the potential of the electrolyte with respect to the photoelectrode. The ITO back electrode was connected as the working electrode. A potentiostat (Metrohm PGSTAT 204) was used for transient current measurements and electrochemical impedance spectroscopy. For spectroscopic measurements a Xenon lamp (Hamamatsu 150W) combined with a Czerny-Turner monochromator (Cornerstone 260) was used as light source. For other measurements a surface mounted LED (595

nm CREE XPE AMB-L1) was used. Data analysis was done with Matlab (code available upon request). Light intensity was calibrated using a Hamamatsu photodiode (S2281).

Surface photovoltage measurements: Measurements were done with a Park NX10 AFM in KPFM mode. A PPP-NCST-Au probe (Nanosensors, k=7.4 N/m) was operated in non-contact mode at resonance frequency to trace the topography. In parallel a 3V amplitude AC-voltage was applied to the tip to modulate electrostatic forces at 17 kHz. The resulting tip oscillation was nullified by the KPFM feedback circuit applying a DC voltage to the tip. The DC voltage is reported here as the surface voltage. Surface voltages were measured in darkness and during light exposure from below the sample. The difference is the surface photovoltage.

Supporting Information
Supporting Information is available from the Wiley Online Library or from the author.

Received: ((will be filled in by the editorial staff))
Revised: ((will be filled in by the editorial staff))
Published online: ((will be filled in by the editorial staff))

References:

[1]   F. Di Maria, F. Lodola, E. Zucchetti, F. Benfenati, G. Lanzani, *Chem. Soc. Rev.* **2018**, *47*, 4757.

[2]   J. Hopkins, L. Travaglini, A. Lauto, T. Cramer, B. Fraboni, J. Seidel, D. Mawad, *Adv. Mater. Technol.* **2019**, *4*, 1.

[3]   G. Manfredi, E. Colombo, J. Barsotti, F. Benfenati, G. Lanzani, *Annu. Rev. Phys. Chem.* **2019**, *70*, 99.

[4]   L. Ferlauto, M. J. I. Airaghi Leccardi, N. A. L. Chenais, S. C. A. Gilliéron, P. Vagni, M. Bevilacqua, T. J. Wolfensberger, K. Sivula, D. Ghezzi, *Nat. Commun.* **2018**, *9*, 1.

[5]   D. Rand, M. Jakešová, G. Lubin, I. Vebraite, M. David-Pur, V. Derek, T. Cramer, N. S. Sariciftci, Y. Hanein, E. D. Głowacki, *Adv. Mater.* **2018**, *1707292*, 1.

[6]   C. Bossio, I. A. Aziz, G. Tullii, E. Zucchetti, D. Debellis, M. Zangoli, F. Di Maria, G. Lanzani, M. R. Antognazza, *Front. Bioeng. Biotechnol.* **2018**, *6*, 1.

[7]   F. Lodola, V. Rosti, G. Tullii, A. Desii, L. Tapella, P. Catarsi, D. Lim, F. Moccia, M. R. Antognazza, *Sci. Adv.* **2019**, *5*, DOI 10.1126/sciadv.aav4620.

[8]   P. Feyen, E. Colombo, D. Endeman, M. Nova, L. Laudato, N. Martino, M. R. Antognazza, G. Lanzani, F. Benfenati, D. Ghezzi, *Sci. Rep.* **2016**, *6*, 1.

[9]   T. Someya, Z. Bao, G. G. Malliaras, **n.d.**, DOI 10.1038/nature21004.

[10]   M. Kaltenbrunner, T. Sekitani, J. Reeder, T. Yokota, K. Kuribara, T. Tokuhara, M. Drack, R. Schwödiauer, I. Graz, S. Bauer-Gogonea, S. Bauer, T. Someya, *Nature* **2013**, *499*, 458.

[11]   Y. Diao, B. C.-K. Tee, G. Giri, J. Xu, D. H. Kim, H. a Becerril, R. M. Stoltenberg, T. H. Lee, G. Xue, S. C. B. Mannsfeld, Z. Bao, *Nat. Mater.* **2013**, *12*, 665.

[12]   J. Xu, S. Wang, G. N. Wang, C. Zhu, S. Luo, L. Jin, X. Gu, S. Chen, V. R. Feig, J. W. F. To, S. Rondeau-Gagné, J. Park, B. C. Schroeder, C. Lu, J. Y. Oh, Y. Wang, Y. Kim, H. Yan, R. Sinclair, D. Zhou, G. Xue, B. Murmann, C. Linder, W. Cai, J. B.-H. Tok, J. W. Chung, Z. Bao, *Science (80-.).* **2017**, *64*, 59.

[13]   D. Khodagholy, J. N. Gelinas, T. Thesen, W. Doyle, O. Devinsky, G. G. Malliaras, G. Buzsáki, *Nat. Neurosci.* **2014**, *18*, 310.

[14]   M. Marzocchi, I. Gualandi, M. Calienni, I. Zironi, E. Scavetta, G. Castellani, B. Fraboni, *ACS Appl. Mater. Interfaces* **2015**, *7*, 17993.

[15]   I. Tonazzini, E. Bystrenova, B. Chelli, P. Greco, P. Stoliar, A. Calò, A. Lazar, F. Borgatti, P. D'Angelo, C. Martini, F. Biscarini, *Biophys. J.* **2010**, *98*, 2804.

[16]   E. Bystrenova, M. Jelitai, I. Tonazzini, A. N. Lazar, M. Huth, P. Stoliar, C. Dionigi, M. G. Cacace, B. Nickel, E. Madarasz, F. Biscarini, *Adv. Funct. Mater.* **2008**, *18*, 1751.

[17]   T. Cramer, A. Campana, F. Leonardi, S. Casalini, A. Kyndiah, M. Murgia, F. Biscarini, *J. Mater. Chem. B* **2013**, *1*, 3728.

[18]   P. A. Bobbert, A. Sharma, S. G. J. Mathijssen, M. Kemerink, D. M. de Leeuw, *Adv. Mater.* **2012**, *24*, 1146.

[19]   C. M. Proctor, J. Rivnay, G. G. Malliaras, **2016**, 1433.

[20]   J. Rivnay, H. Wang, L. Fenno, K. Deisseroth, G. G. Malliaras, *Sci. Adv.* **2017**, *3*, e1601649.

[21]   F. Decataldo, T. Cramer, D. Martelli, I. Gualandi, W. S. Korim, S. T. Yao, M. Tessarolo, M. Murgia, E. Scavetta, R. Amici, B. Fraboni, *Sci. Rep.* **2019**, *9*, 1.

[22]   S. Fabio, D. Fonzo, M. Rosa, S. Leonardi, M. T. Mayer, M. Schreier, M. Gra, G. Lanzani, F. Di Fonzo, M. R. Antognazza, *Energy Environ. Sci* **2016**, *9*, 3710.

[23]   D. Hursan, A. Kormanyos, K. Rajeshwar, C. Janaky, *Chem. Commun.* **2016**, *52*, 8858.

[24]   T. Yohannes, T. Solomon, O. Inganäs, *Synth. Met.* **1996**, *82*, 215.

[25]   J. Desilvestro, O. Haas, *Electrochim. Acta* **1991**, *36*, 361.

[26]   P. A. Kilmartin, G. A. Wright, *Electrochim. Acta* **1998**, *43*, 3091.

[27]   M. Gryszel, A. Markov, M. Vagin, E. D. Głowacki, *J. Mater. Chem. A* **2018**, *6*, 24709.

[28]   M. Gryszel, M. Sytnyk, M. Jakešová, G. Romanazzi, R. Gabrielsson, W. Heiss, E. D. Głowacki, *ACS Appl. Mater. Interfaces* **2018**, *10*, 13253.

[29]   M. Jakešová, M. Silverå Ejneby, V. Đerek, T. Schmidt, M. Gryszel, J. Brask, R. Schindl, D.

T. Simon, M. Berggren, F. Elinder, E. D. Głowacki, *Sci. Adv.* **2019**, *5*, eaav5265.

[30]   M. Gryszel, E. D. Głowacki, *Chem. Commun.* **2020**, *56*, 1705.

[31]   A. Giovannitti, R. B. Rashid, Q. Thiburce, B. D. Paulsen, C. Cendra, K. Thorley, D. Moia, J. T. Mefford, D. Hanifi, D. Weiyuan, M. Moser, A. Salleo, J. Nelson, I. McCulloch, J. Rivnay, *Adv. Mater.* **2020**, *32*, 1.

[32]   A. Kyndiah, T. Cramer, C. Albonetti, F. Liscio, S. Chiodini, M. Murgia, F. Biscarini, *Adv. Electron. Mater.* **2015**, *1*, 1400036.

[33]   E. M. Tennyson, J. L. Garrett, J. A. Frantz, J. D. Myers, R. Y. Bekele, J. S. Sanghera, J. N. Munday, M. S. Leite, *Adv. Energy Mater.* **2015**, *5*, 1.

[34]   R. Memming, *Semiconductor Electrochemistry*, Weinheim, **2015**.

[35]   A. Sugie, W. Han, N. Shioya, T. Hasegawa, H. Yoshida, *J. Phys. Chem. C* **2020**, *124*, 9765.

[36]   K. Krumova, G. Cosa, in *Singlet Oxyg. - Appl. Biosci. Nanosci.*, The Royal Society Of Chemistry, **2016**, pp. 5–18.

[37]   R. van de Krol, M. Grätzel, *Photoelectrochemical Hydrogen Production*, **2012**.